Journal of Magnetism and Magnetic Materials 556 (2022) 169440

Contents lists available at ScienceDirect

Journal of Magnetism and Magnetic Materials

journal homepage: www.elsevier.com/locate/jmmm

Functional properties of Yttrium Iron Garnett thin films on graphene-coated $Gd_3Ga_5O_{12}$ for remote epitaxial transfer

S. Leontsev [a,b], P.J. Shah [a], H.S. Kum [c,f], J.L. McChesney [d], F.M. Rodolakis [d], M. van Veenendaal [d,e], M. Velez [a], R. Rao [a], D. Haskel [d], J. Kim [c], A.N. Reed [a], M.R. Page [a,*]

[a] Materials and Manufacturing Directorate, Air Force Research Laboratory, WPAFB, OH 45433, USA
[b] UES Inc., Dayton, OH 45432 USA
[c] Department of Mechanical Engineering, Massachusetts Institute of Technology, Cambridge, MA 02139, USA
[d] X-ray Science Division, Advanced Photon Source, Argonne National Laboratory, Lemont, IL 60439, USA
[e] Department of Physics, Northern Illinois University, De Kalb, IL 60115, USA
[f] Department of Electrical and Electronic Engineering, Yonsei University, Seoul, South Korea

ARTICLE INFO

Keywords:
YIG thin films
Remote epitaxy
FMR
Gilbert damping

ABSTRACT

Remote epitaxial growth via a graphene interlayer and subsequent mechanical exfoliation of a free-standing membrane is a recently developed technique used to transfer complex oxide thin films onto non-native substrates to form heterogeneously integrated structures for various device applications. One such oxide is Yttrium Iron Garnet (YIG), a material of choice for a wide range of magnetoelectric and spintronic devices owing to its ferromagnetism with high Curie temperature as well as high quality factor and low losses in microwave frequencies. YIG is predominantly grown on lattice matched Gadolinium Gallium Garnet (GGG) substrates, but by utilizing the remote epitaxy technique, high quality YIG films can be transferred from GGG onto another substrate such as piezoelectric Lithium Niobate (LN). Mechanical strain coupling between the layers and magnetostrictive nature of YIG would allow for the investigation of the interplay in YIG/LN structures leading to the design of novel frequency agile magneto-acoustic devices. In this study functional properties of a YIG film grown using PLD on graphene-coated GGG substrate were investigated and compared to traditional YIG on GGG. Both materials were characterized in terms of crystal structure, surface morphology, FMR and Gilbert damping, and Raman and XAS spectroscopy. It was found that YIG on graphene-coated GGG exhibits significantly higher microwave losses than standard YIG on GGG (FMR linewidth 30.9 vs 2.1 Oe at 10 GHz, and Gilbert damping coefficient 15.4×10^{-4} vs 3.4×10^{-4} respectively), which was attributed to increased concentration of Fe^{2+} cations in YIG/Graphene/GGG. While the damping is higher in these studied films compared to YIG grown directly on GGG, the resulting properties are still very favorable compared to many other competing materials which can be grown without the need for lattice matched substrates, such as metallic ferromagnets.

1. Introduction

Multiferroics are a class of materials simultaneously exhibiting more than one ferroic property, such as ferromagnetism, ferroelectricity or ferroelasticity. These materials present significant research interests due to realization of magnetoelectric (ME) coupling, which allows direct manipulation of electric polarization through applied magnetic field, or, conversely, control of material magnetization via electric field. Most prominently the ME coupling is observed in thin film multiferroic composites consisting of piezoelectric and magnetostrictive layers. In such structures magnetization and polarization are strain-mediated due to strong mechanical clamping at the interface, any change in lattice parameter in one phase translates into the other bridging their ferroic properties [1–4].

Research progress in the area of multiferroic composites has led to development of novel multifunctional devices that utilize efficient magnetoelectric coupling. Thin film structures based on piezoelectric ZnO, AlN, AlScN, PZN-PT or magnetostrictive Metglass, FeGaB, FeGaC, CoFeC [5–13] materials have been investigated for practical applications in devices such as ME antennas, sensors, energy harvesters, magnetoelectric random access memory, tunable RF components etc [14]. In microwave applications the ferromagnetic component of the ME

* Corresponding author.
E-mail address: michael.page.16@us.af.mil (M.R. Page).

https://doi.org/10.1016/j.jmmm.2022.169440
Received 15 February 2022; Received in revised form 18 April 2022; Accepted 30 April 2022
Available online 5 May 2022
0304-8853/Published by Elsevier B.V.

device often operates at resonance conditions. For example, in a tunable filter device, the resonance condition indicates which frequency is filtered or blocked from the frequency spectrum of the filter device. Quality factor (Q) of the resonance condition is governed by the microwave loss or FMR (ferromagnetic resonance) line width of the ferromagnetic thin film. Recently several reports have shown the effectiveness of acoustic excitation of resonance condition in these thin film magnetoelectric composites [15,16]. Our recent study on a variety of magnetic materials (i.e. FeCo, FeCoGd, FeGaB, FeCoSiB) via the acoustically driven FMR (ADFMR) showed that each of these materials displays its own ADFMR signature [17,18] and how these materials attributes could lead to the design of next generation surface acoustic wave (SAW) based frequency agile magnetoacoustic filters.

Ideally it is desired that the magnetic layer of the ME system has large magnetostriction constant, low coercivity, and narrow FMR linewidth. One of the materials with the lowest microwave damping is Yttrium Iron Garnett (YIG). Single crystalline YIG thin films have been extensively studied for potential application in spintronics, magnonics and related applications exploiting magnetization dynamics due to exceptionally narrow FMR linewidth, low Gilbert damping coefficient and strong magnetic properties [19–23]. Although the magnetostriction constant in YIG is relatively low (only 2–4 $\times$ 10^{-6} ppm) [24] it can still be very impactful to integrate ultra-high quality single crystalline YIG thin films in a magnetoelectric ADFMR device on a $LiNbO_3$ (LN) platform similarly to the above mentioned FeCo-based system. The high Q resonance in YIG films offers a unique ability for the design of frequency-notch or band-stop magneto-acoustic tunable devices.

Complex oxide films such as garnets and ferrites are usually grown by various deposition techniques - liquid phase epitaxy [25], magnetron sputtering [26,27], pulsed laser deposition [22,28]. In order to produce high-quality crystalline films these traditional heteroepitaxy methods require a close match between film and substrate lattice constants. Oxides grown on non-lattice matched substrates tend to have poor functional properties, which limit the exploration of these films on device-friendly substrates. The substrate of choice for epitaxial YIG film growth is GdGa-garnet (GGG) due to its exceptionally close lattice constant match (difference less than 0.05%). On the other hand, attempting to deposit YIG directly onto piezoelectric $LiNbO_3$ for ADFMR device fabrication will result in a poor quality film and thus poor functional properties [29]. Therefore a different solution is needed for the integration of YIG on lithium niobate without compromising its crystalline quality and low microwave damping.

Recently a technique was shown to effectively transfer epitaxial quality complex oxide thin films on non-lattice matched substrates for magnetoelectric device applications. This technique utilizes remote epitaxial growth of the film of interest on its native substrate via a graphene interlayer and subsequent mechanical exfoliation of a free-standing single crystalline membrane [30–32]. The exfoliated membranes can be used to build a stacked structure joining two materials with a large lattice mismatch or a unique property combination. Furthermore, being removed from a substrate, these artificial heterostructures become free from the substrate clamping effects which significantly limit piezoelectric or magnetostrictive properties of the constituent materials.

Remote epitaxial growth of YIG on graphene-coated GGG substrate has been successfully attempted earlier and single crystal YIG membranes with uniform out-of-plane orientation were demonstrated [31]. These are encouraging results and using the remote epitaxy technique opens up a possibility of high quality YIG film transfer onto $LiNbO_3$ and fabrication of an ADFMR device. However, magnetic properties and microwave damping have not been evaluated for the remote epitaxial YIG. It is still unclear if the presence of graphene as an interlayer between YIG and GGG negatively affects the magnetic response in YIG, which may affect the overall ADFMR device performance after YIG exfoliation and transfer.

The objective of our present work is to use this remote epitaxy method and develop the process to transfer YIG (and later NiZnAl-ferrite) thin films onto our $LiNbO_3$-based ADFMR devices. As a first step, we have acquired graphene monolayer thin films on GGG substrates and completed growth of epitaxial YIG films on GGG substrate with and without graphene monolayers. Subsequently we assessed the performance of both films to truly understand the effect of monolayer graphene on YIG films functional properties. Evaluation and comparison of FMR signatures, Gilbert damping, surface and crystalline quality, ion valence state balance between YIG films produced with and without the graphene interlayer are reported in this paper.

2. Experimental

YIG thin films were epitaxially grown on bilayer graphene-coated high quality GGG (1 1 1) substrates in a custom built ultra-high vacuum PLD system. Details on the graphene growth and transfer process can be found in work by Kim *et al.* [32]. The samples were placed into the PLD growth chamber via a load-lock under the base pressure of 10^{-7}-10^{-8} Torr and heated to 775 °C at a rate of 20 °C/min using a contactless heater and temperature control based on the sensor reading at the back of the heated substrate holder. YIG growth was carried out using a $\lambda =$ 248 nm excimer laser (Lambda Physik LPX 305i) at fluency $\sim$ 2.7 J/cm^2 and 4 Hz pulse rate at a partial oxygen pressure of 100 mTorr. Laser power and pulse count were adjusted to obtain $\sim$ 80 nm thick film. Prior to the deposition the 1-in diameter YIG target was pre-ablated for 2 min with a target to substrate distance of 6 cm. After the deposition the samples were cooled down to room temperature at 10 °C/min rate, removed from the PLD chamber and later annealed in oxygen at 875 °C for 1 h in a separate furnace. Additionally, another YIG sample was deposited on an identical graphene-coated GGG substrate at 875 °C but without any subsequent annealing. For each growth condition a control YIG sample was also prepared on bare (non-graphene coated) GGG substrate for property comparison.

Crystal structure of the YIG films was characterized with high-resolution X-ray diffractometry on a PANalytical X'Pert PRO instrument equipped with a Cu k-α radiation source, hybrid Ge(2 2 0) monochromator and point scintillation detector. XRD scan range $2\theta = 48$ thru 53° was selected to capture the film YIG (4 4 4) and substrate GGG (4 4 4) diffraction peaks.

The FMR measurements were conducted with the samples placed face down on a broad band coplanar waveguide located in the middle of a scanning DC field electromagnet (GMW, model 3473-MRD). Sample was orientated in-plane with the applied magnetic field and exposed to excitation microwave signal at set frequencies up to 40 GHz (Keysight EXG analog signal generator, N5173B) superimposed with a weak low-frequency modulation AC field. The response (microwave power absorption rate) was detected with a lock-in amplifier (SRS, SR860) as a function of sweeping DC magnetic field. Each FMR signature was fit with a Lorentzian peak derivative function to extract the resonance field H_P and the half-width at half-maximum (HWHM) linewidth ΔH.

Morphological properties of both YIG samples were investigated with AFM technique using Asylum Research scanning probe microscope with high spatial and depth resolution.

X-ray absorption spectroscopy (XAS) experiments were performed at beamline 29-ID of the Advanced Photon Source, Argonne National Laboratory. The beamline is equipped with a variable line spacing (VLS) ruled grating Si monochromator [33] with an experimental resolution $\sim$ 100 meV. Data were collected in two modes - total fluorescence yield (TFY) and total electron yield (TEY), however, only the TFY mode was deemed reliable due to the insulating nature of the YIG material.

Raman spectral maps were collected in a Renishaw Raman microscope with an excitation wavelength of 633 nm. Focusing was done with a 100x objective lens (corresponding to a spot size of 1 um). Two-dimensional Raman maps were collected over 20 $\times$ 20 um regions, with step sizes of 1 um. Spectra were collected with 3 s acquisition times and 2 accumulations, and the laser power was kept low ($\sim$1 μW) to

avoid laser heating. Analysis of the maps was performed in the Renishaw Wire software to generate 2D intensity maps as shown later in the main text.

Crystallographic orientation analysis was conducted with a FEI Quanta 600 FEG scanning electron microscope (SEM) equipped with an EDAX Hikari electron backscatter electron (EBSD) camera. This analysis was conducted using a 20 kV accelerating voltage with spot size of 5 and scan resolution (step size) of 6 μm. Due to the insulating nature of the materials the microscope was run in low vacuum mode, where water vapor was introduced into the chamber at 0.13 mbar to mitigate charge accumulation on the sample surface. This approach provided the necessary beam stability without the usual method of coating with noble metal, which would interfere with the diffracted signal. The post-acquisition data processing was performed using EDAX OIM V7 software to produce EBSD pole figures and inverse pole figure (IPF) maps for displaying the crystallographic orientation at the surface of the sample.

3. Results and discussion

3.1. X-ray diffraction (XRD)

Crystalline structure of the first YIG films grown on graphene and on bare GGG substrate at 775 °C was probed with X-ray diffraction and compared (Fig. 1a). Since the growth temperature of 775 °C for these films was much lower than the optimal substrate temperature we didn't observe YIG phase resolved in the XRD spectra of both as-grown YIG/GGG and YIG/Graphene/GGG samples. After annealing at 875 °C the YIG (444) peak in YIG/Graphene/GGG sample became visible indicating formation of the YIG phase (Fig. 1b). However, the broadness of this peak and absence of Laue fringes suggest poor crystalline quality of the film, which is additionally corroborated by the lack of FMR signal from YIG in either of the two samples.

Subsequently we increased the substrate growth temperature to 875 °C and deposited YIG on Graphene/GGG substrate at conditions identical to the optimal YIG growth on bare GGG. No annealing was done on these samples. The new films showed well defined crystalline structure in XRD (Fig. 1c) with YIG (444) peaks present on both Graphene/GGG and control bare GGG samples. Strong Laue fringes in the case of the control YIG sample are indicative of a high crystalline quality film with well-defined crystallographic layers and high ordering. On the other hand, the slightly lower peak intensity and weaker Laue oscillations in the YIG/Graphene/GGG sample suggest degradation in the film crystallinity and surface quality, which is also supported by AFM results (Fig. 6) revealing 10 times higher surface roughness and defect density for the graphenated films. Based on the fringe periodicity the YIG thickness in both samples was estimated at approximately 80 nm. Close similarity in thickness between the above two samples points to similar growth kinetics (at identical PLD conditions) even with the graphene present in the YIG/Graphene/GGG sample. It is possible to expect the YIG nucleation process to be different on the graphene-coated GGG, which would alter the overall thickness of the film. However, as supported by DFT calculation results from Kum[31], the bilayer graphene used in our experiments does not significantly affect atomic potential field of the substrate allowing for similar YIG nucleation process as in the case of bare substrate.

Unlike YIG films grown at 775 °C, the FMR signal was detected for the films grown at 875 °C and we were able to quantify the FMR linewidth broadening as a function of frequency for the YIG/Graphene/GGG sample as discussed in the next section.

3.2. Ferromagnetic resonance (FMR)

We measured the FMR microwave properties of YIG/Graphene/GGG and control YIG/GGG samples. There was no FMR signal detected in our first set of samples (grown at 775 °C), including the YIG on graphene-coated substrate after annealing. However, the second set (grown at 875 °C) showed distinct FMR response. Example FMR signatures measured from both YIG/Graphene/GGG, and control sample are shown in Fig. 2. Typical results extracted from these measurements are FMR peak-to-peak linewidths ΔH_{pp}, which are characteristics of magnetic damping in the material. YIG is like a gold-standard for low magnetic damping and is the most favored attribute for microwave device applications allowing higher sensitivity and more stable signal processing [19,20]. The standard YIG on bare substrate showed $\Delta H_{pp} = 2.1$ Oe at 10 GHz excitation frequency, this value is among the lowest reported in the literature for sub 100 nm YIG thin films [21] and has consistently been achieved in our previous experiments based on the PLD growth optimization [22].

On the contrary, ΔH_{pp} in the graphenated YIG sample showed a much higher value of 30.9 Oe (at 10 GHz). Large FMR linewidth observed in YIG on graphene-coated GGG indicates potential degradation in quality of the film compared to control YIG, which could depend on a number of characteristics such as stoichiometry, film surface uniformity, grain structure, defect concentration etc. Even though the increased damping is not desired for practical YIG applications we still consider this a promising result since our measurable FMR response in this novel YIG/Graphene/GGG structure is being reported for the first time. Furthermore, we tried to investigate the root cause of the increased damping in YIG on graphene-coated GGG in a series of measurements presented below.

FMR frequency sweep measurements were performed on both samples to investigate dependence of the FMR linewidth and resonant field on frequency (Fig. 3). Theoretically the field-swept FMR linewidth is proportional to the Gilbert damping constant α, which is an intrinsic

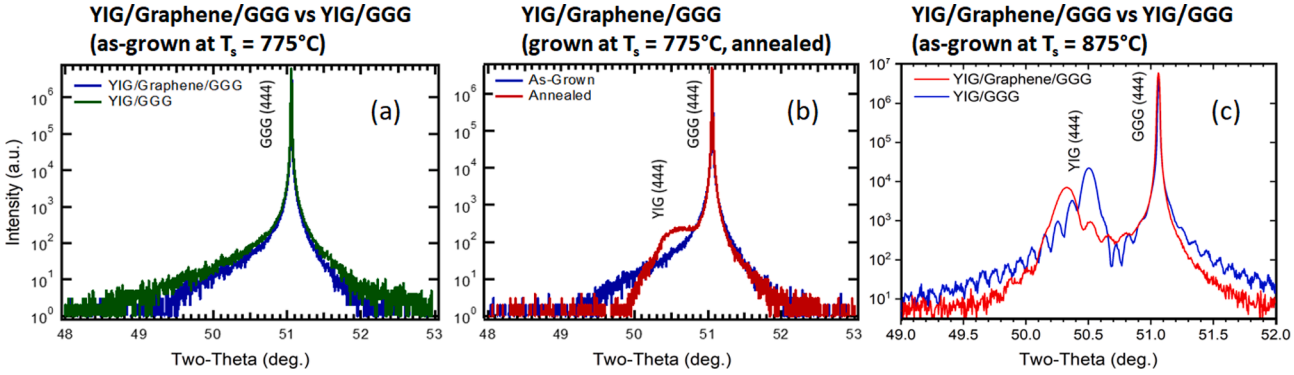

Fig. 1. (a) Initial XRD spectra of YIG/GGG and YIG/Graphene/GGG films grown at 775 °C substrate temperature, no YIG peaks are observed indicating amorphous nature of the films; (b) Comparison between as grown (at 775 °C) and annealed (at 875 °C) YIG/Graphene/GGG samples, onset of YIG phase formation is evident in the annealed sample; (c) XRD data comparison for the YIG/GGG and YIG/Graphene/GGG films grown at 875 °C; both samples show well-defined crystalline YIG peaks and Laue fringes.

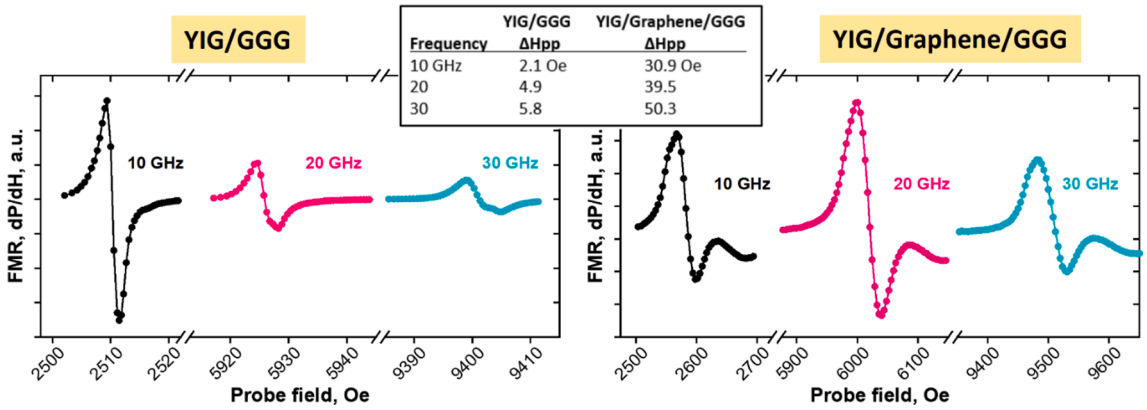

Fig. 2. Example FMR curves for YIG/GGG (left) and YIG/Graphene/GGG (right) measured at 10, 20 and 30 GHz. FMR linewidth for the two samples is shown in the inset table. The distinct FMR response from YIG on graphenated GGG is being reported for the first time, displaying significantly larger FMR linewidth than YIG on GGG.

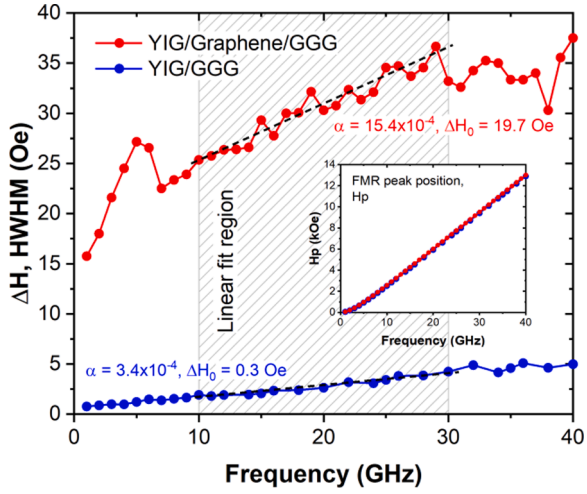

Fig. 3. Frequency dependence of the FMR linewidth (ΔH, HWHM) and resonance field (H_P) for the YIG/GGG and YIG/Graphene/GGG films. Linear fit was applied to ΔH vs frequency data in order to extract Gilbert damping coefficient and inhomogeneous broadening parameter for both samples.

measure of how fast the spin precession around an applied magnetic field decays over time. It has a linear dependence on the FMR frequency, which can be approximated by the following equation (1) in the Landau-Lifshitz model [34]:

$$\Delta H = \Delta H_0 + \frac{\alpha}{\gamma} f \quad (1)$$

where ΔH is the FMR linewidth (half-width at half-maximum, HWHM), f is frequency in MHz, $\gamma = 2.8$ MHz/Oe is the gyromagnetic ratio. A linear fit was applied to our experimental data (in the range between 10 and 30 GHz) in order to extract the Gilbert damping coefficient α and the inhomogeneous broadening ΔH_0. The calculated fitting parameters were $\alpha = 15.4 \times 10^{-4}$, $\Delta H_0 = 19.7$ Oe (for YIG/Graphene/GGG) and $\alpha = 3.4 \times 10^{-4}$, $\Delta H_0 = 0.3$ Oe (for YIG/GGG). The Gilbert damping coefficient for our control YIG on bare GGG is well within the range of 1–5 $\times 10^{-4}$ reported for other high quality YIG thin films with thickness below 100 nm, and the inhomogeneous contribution ΔH_0 is one of the lowest reported [21,35].

Comparing the above numbers we can see that the linewidth broadening in YIG/Graphene/GGG is dominated by the external non-homogeneous parameter ΔH_0. This contribution is related to the sample inhomogeneity due to local variation of magnetization, various surface or interface non-uniformities and defects. In other words, if different parts of the sample have dissimilar FMR response then the cumulative FMR peak would be broadened. Large value of ΔH_0 is consistent with the inferior film crystalline quality observation based on the XRD data and higher surface roughness observed with AFM. The Gilbert damping coefficient α is also higher for the YIG on graphene. Although the origin of Gilbert damping is not well understood, factors like strength of the spin–orbit coupling and local deviations of the ionic charge state do impact damping in these films. We hypothesize that graphenated YIG film may contain regions with Fe^{2+} cation presence instead of purely Fe^{3+}, which degrades and broadens the FMR response and thus increases damping. To confirm this hypothesis XAS measurements are discussed below in the next section.

3.3. X-ray absorption spectroscopy (XAS)

XAS is a powerful technique that allows characterization of the local environment around the probing atoms and can be used to distinguish the chemical species and oxidation states of Fe, i.e. it is a direct measure of the element valence state [36,37]. Analysis of these data will quantitatively give us information on Fe^{2+}: Fe^{3+} ratio in control YIG and graphenated YIG films and thereby confirm our hypothesis for the cause of increased damping.

Our experimental XAS data probing the Fe-$L_{2,3}$ edges are shown in Fig. 4. The TFY lines for the YIG/GGG represent a typical response from

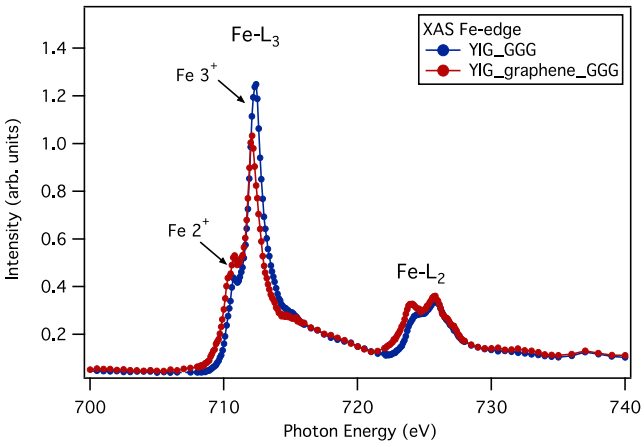

Fig. 4. XAS spectra of YIG/GGG and YIG/Graphene/GGG thin films taken in fluorescence yield. The spectra indicate the differences in the Fe^{2+} and Fe^{3+} ions in the complex oxide film which may explain the increase in damping in the YIG/Graphene/GGG film.

Fe showing main Fe^{3+} peak around 712 eV. A weak shoulder on edge at 710 eV is indicative of Fe^{2+} but it also overlaps with a small peak with similar energy due to multiplet structure of Fe^{3+} in octahedral sites. The data for the graphenated YIG is similar in spectral features, however, noticeable increase in the edge shoulder and decrease in the main Fe^{3+} peak intensity implies presence of the Fe^{2+} component. Additionally there is a slight shift of the L-edges towards lower photon energy. These findings point to potential deviation from YIG stoichiometry in the graphenated sample, which in turn contributes to the increased microwave damping observed in the FMR measurements earlier.

To quantify the XAS results more accurately we performed additional analysis by fitting the experimental data with a linear superposition of theoretical XAS spectra for each Fe^{+} state expected in the YIG crystal structure (i.e. tetrahedral and octahedral sites, Fe^{2+} and Fe^{3+} valence states, in an ideal YIG only the Fe^{3+} states are expected). This type of fitting has shown to provide insight on Fe^{+} ionic charge content in other systems like magnetite, hematite, and also in complex oxides [38,39]. We applied this technique to estimate any deviation from stoichiometry in the present graphenated YIG and control YIG samples.

Fig. 5 shows the fitting results for both samples. Control YIG was modelled by taking theoretical XAS curves [40] for the Fe^{3+} octahedral (Oh) and tetrahedral (Td) sites in the known ratio 2:3 and fitting them to match the intensity of the main Fe-L_3 edge (~712 eV). Although stoichiometric YIG only has Fe^{3+} ions, we allowed for possible off-stoichiometry by adding Fe^{2+} curves (also in the 2:3 Oh:Td ratio) to the linear combination to adjust for the pre-peak feature at 711 eV. Double step background approximated by arctangent function was also included. With the best match to the experimental data the simulations indicate that the control YIG film consists of 91% Fe^{3+} with a 9% contribution of Fe^{2+} states. Ideally in the crystalline YIG film we would expect only the Fe^{3+} content, however, since the TFY measurement probes the full thickness of the film the cation ratio is averaged over the entire sample and the 9% Fe^{2+} contribution could originate from regions such as interface or surface with much larger Fe^{2+} content.

An analogous approach was taken for the graphenated YIG sample. In this case, the Fe^{2+} content was estimated at 29%, which is significantly higher than in the control YIG on bare GGG. We believe that higher concentration of Fe^{2+} in the graphenated YIG could occur due to several reasons. Initial coating of the GGG substrate with graphene involves a transfer process using PMMA and there is a possibility of the organic residue present on the graphene surface after the transfer. This may affect the chemistry of YIG at the interface region but not necessarily in the rest of the film. Another possible reason is graphene oxidation occurring as the substrate is heated to high temperature (875 °C) in partial O_2 atmosphere just before YIG deposition. We speculate that the above factors can result in the shift of Fe^{+} ion balance but with the majority of the Fe^{2+} concentrating in the vicinity of the YIG/substrate interface and the rest of the film having the desired YIG stoichiometry. Since the XAS probes the whole thickness of the film we still see the Fe^{2+} presence in the spectral intensity data.

As described earlier, the YIG/Graphene/GGG sample exhibits significantly increased FMR linewidth broadening compared to standard YIG (ΔH_{pp} of 30.9 vs 2.1 Oe respectively at 10 GHz). Our XAS results indicate evidence of strong deviations in Fe^{+} balance and charge relaxation process, which we can attribute to the increased loss in the graphenated YIG. This mechanism is also called the valence-exchange relaxation and occurs in crystals with Fe^{2+} and Fe^{3+} ions on equivalent sites, its physical origin is 3*d*-electron hopping between the Fe ions [41,42].

3.4. Atomic force microscopy (AFM)

Surface morphology of both control YIG and graphenated YIG samples were investigated with AFM technique (Fig. 6). AFM topography has not shown any significant surface variations in the control YIG sample, and the AFM contrast was uniform with RMS roughness lower than 0.2 nm, which is less than the lattice parameter and is on par with other high quality YIG films reported in literature [22,35]. These findings indicate good surface quality of the control YIG film and are consistent with the observed low loss in the FMR measurements. On the other hand, the graphenated YIG film showed significantly higher surface roughness and inhomogeneity (RMS roughness 2.2 nm with spikes over 20 nm high). It might appear that the graphene surface on GGG substrate has non-idealities which may translate into further defects in the YIG grown on top. For example, discontinuities in the graphene layer could lead to polycrystalline nature of the YIG film and thus cause increased FMR linewidth broadening due to variation of crystallographic orientation between individual grains and defects on their boundaries. Based on the above AFM observations we decided to investigate the quality of the underlying graphene layer with Raman spectroscopy. This Raman mapping of graphene-coated GGG sample was done on a different sample without YIG film growth. The graphene growth and transfer on GGG substrate is presumably identical in this sample as compared to the graphenated YIG sample.

3.5. Raman spectroscopy

To confirm the assumption whether there are inhomogeneities within the graphene layer on GGG substrate we performed confocal Raman mapping of the graphene/GGG surface (prior to growing YIG). Raman spectroscopy is an essential tool for investigation of properties of graphene [43]. It is relatively simple and allows non-destructive detection of chemical modifications, structural damage, local stress and strain, atomic structure and electronic properties among many other uses. The graphene Raman spectrum features two distinct bands: 2D and G; the intensity and position of these bands measured across the graphene surface provide specific information such as layer thickness and interlayer orientation [44].

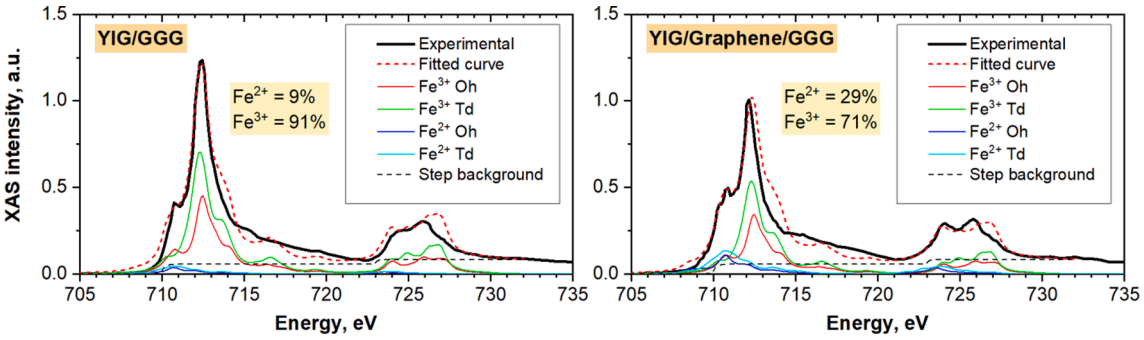

Fig. 5. Experimental XAS data fitting for YIG/GGG and YIG/Graphene/GGG using linear combination of theoretical spectra for individual Fe^{+} states. The YIG on graphenated GGG shows higher proportion of Fe^{2+} ions, which is believed to cause deviations from stoichiometry and contribute to the increased damping in this sample.

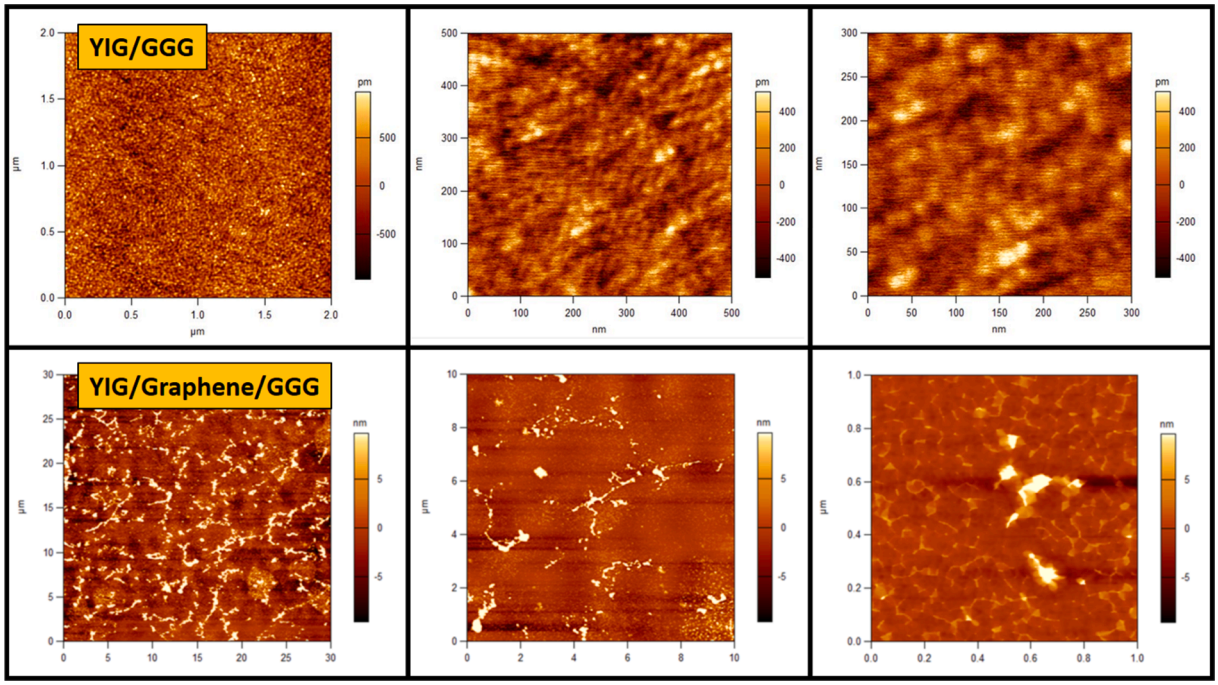

Fig. 6. (top row) AFM images of the YIG/GGG film showing very smooth surface, RMS roughness below 0.2 nm; (bottom row) AFM images of the YIG/Graphene/GGG revealing strong non-uniformities (up to 20 nm in height), surface RMS roughness of 2.2 nm.

The Raman mapping results measuring G and 2D band intensity as well as their ratio 2D/G are shown in Fig. 7. The G and 2D bands are labeled and all other peaks correspond to GGG. We observed primarily uniform spatial peak intensity distribution, and particularly it is important to note the uniformity of the 2D/G ratio since it is closely related to the number of graphene monolayers. These results indicate that graphene surface is pristine and possibly less likely to cause excessive surface roughness in graphenated YIG films. However, the spatial resolution of Raman mapping was only around ~ 1 μm per step, which might be too low to detect any surface defects on the nanoscale. In fact the AFM data presented earlier in the paper (Fig. 6) reveal features on YIG/Graphene/GGG surface around 100 nm in size imaged at nm-scale resolution. These may originate from the imperfections in the underlying graphene not visible by Raman due to limited mapping resolution. In addition, the Raman mapping was performed only at room temperature before the YIG deposition (at 875 °C) and it does not reflect any temperature-related changes in the graphene surface quality.

In our experience we were able to deposit high quality smooth YIG films on GGG substrates using optimized PLD growth conditions. In the case with the YIG on graphenated GGG the significant film surface roughness is definitely due to the presence of the graphene interlayer. As mentioned previously in the discussion there is a chance of residual PMMA remaining on the graphene surface after the substrate coating process. These residual organics will affect the surface roughness of the

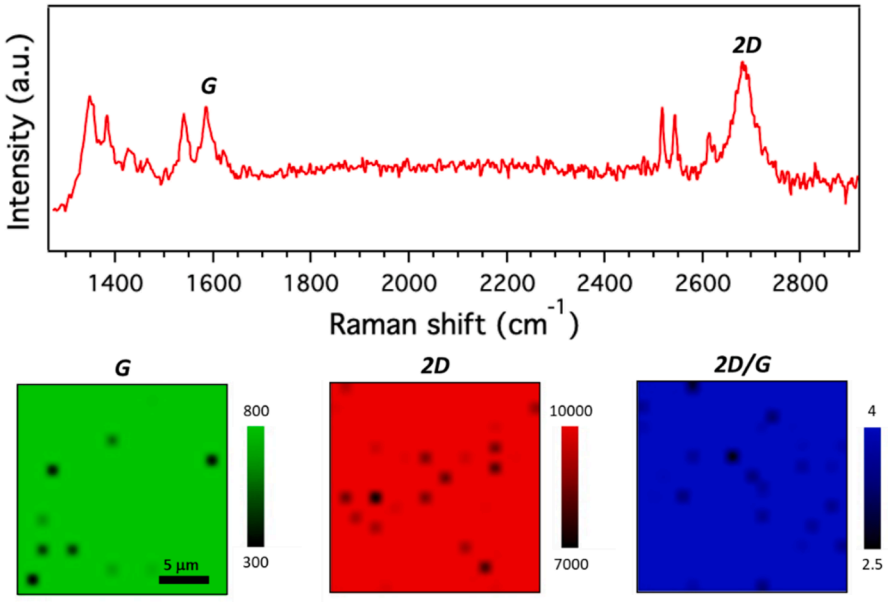

Fig. 7. Raman mapping of Graphene/GGG surface to assess the quality of graphene layer. Example spectrum (top) and G, 2D and 2D/G spatial maps (bottom). The observed uniform spatial peak distribution is indicative of pristine graphene surface.

subsequently grown YIG film. Additionally, the graphene layer may lose its surface integrity because of the large difference in thermal expansion coefficients compared to GGG substrate ($\alpha_{GGG} = 9.2 \times 10^{-6}\ K^{-1}$, $\alpha_{graphene\ bilayer} = -3.4 \times 10^{-6}\ K^{-1}$) [45] during the heating process, which may cause graphene wrinkling and will affect the surface quality of the deposited YIG as well.

3.6. Electron backscatter diffraction (EBSD)

Electron backscatter diffraction (EBSD) is a technique that allows crystallographic orientations, misorientations, texture trends and grain boundary types to be characterized and quantified on a sub-micron scale using scanning electron microscope (SEM) [46]. Applying this analysis to the YIG/GGG and YIG/Graphene/GGG films will allow an additional insight into the crystalline quality of our samples. This technique is highly surface sensitive with the data being collected from the depth of only few tens on nanometers, which in turn is well suited for investigating the present YIG films with the thickness around 80 nm.

Inverse pole figure maps were plotted for both samples (Fig. 8) spanning an area of a few mm^2. For the standard YIG/GGG these results show highly uniform ⟨1 1 1⟩ crystallographic orientation (color coded in blue) throughout the whole area. More detailed texture analysis using pole figures reveals exceptionally well-textured film in {1 1 1} direction all together suggesting excellent YIG crystalline quality. The YIG/Graphene/GGG film also showed uniform ⟨1 1 1⟩ orientation without any visible deviations over large area and similar well-defined pole figure features indicating very good crystallographic alignment along {1 1 1} direction. Worth noting is a slight (~3°) misfit of the central [1 1 1] pole figure marker with respect to the center of the figure, which can be most likely attributed to sample alignment error during mounting on the SEM stage. This could be further verified by reciprocal space mapping measurements using XRD in order to rule out the misorientation between YIG and GGG substrate.

A minor difference of 0.3% between the YIG/GGG and YIG/Graphene/GGG crystallographic (4 4 4) plane spacing was detected earlier by XRD (Fig. 1) and we expected it to be reflected in the EBSD pole figures as well. We looked at the angular spacing between {1 0 0} pole figure markers using the EBSD software to quantify a potential difference in lattice strain between the two samples. The angles were measured 90.11 ± 0.22° and 90.08 ± 0.29° for YIG/GGG and YIG/Graphene/GGG respectively, and within the given error bars we could not resolve any mismatch.

The above EBSD mapping results clearly show that presence of graphene was not detrimental to highly textured epitaxial YIG growth, and the crystallographic alignment of the YIG/Graphene/GGG is nearly identical to its standard counterpart.

4. Summary and conclusion

In this study we demonstrated PLD growth of a YIG film on a graphenated GGG substrate as a step towards remote epitaxial transfer of highly crystalline YIG film from GGG substrate onto other device-friendly substrates (such as Lithium Niobate). The key aspect of this process is to maintain pristine crystallinity of YIG films with exceptionally low damping when separated from its native GGG substrate. However, even the initial growth of YIG on graphene proved to be challenging. Our films deposited on graphene at optimal PLD conditions showed average crystalline quality in the XRD measurements (evidenced by broad peak and weak Laue fringes) and significantly higher FMR linewidth broadening compared to the control YIG/GGG. We conducted a series of experiments to gain understanding of the root cause of such large damping in YIG on graphenated GGG.

FMR frequency sweep analysis showed that there is a strong non-homogeneous component to the linewidth broadening in YIG/Graphene/GGG sample, likely as a result of crystalline defects and surface roughness. Gilbert damping coefficient is also higher compared to the control YIG, which could stem from stoichiometry deviations and unwanted change in Fe^{+} ion balance. AFM topography revealed significant roughness of the new YIG film, but interestingly enough, the initial graphene layer prior to YIG deposition seems to be in pristine shape according to confocal Raman mapping, and the YIG grown on graphene preserved its preferred (1 1 1) out-of-plane orientation as seen in EBSD analysis. Valence state of Fe^{+} was also probed with XAS technique, and in fact these results showed noticeable increase of the Fe^{2+} to Fe^{3+} ratio in the YIG/Graphene/GGG sample.

The above discussed data under this study suggests that the functional properties of YIG films grown on graphene monolayer degraded due to the deviation in stoichiometry and high Fe^{2+} to Fe^{3+} ion ratio in the films and thereby transferred YIG films will have degraded functional properties as well. Substrate growth temperature may very well be a contributing factor for these phenomena.

CRediT authorship contribution statement

S. Leontsev: Writing – original draft, Formal analysis, Investigation. **P.J. Shah:** Conceptualization, Formal analysis, Supervision. **H.S. Kum:**

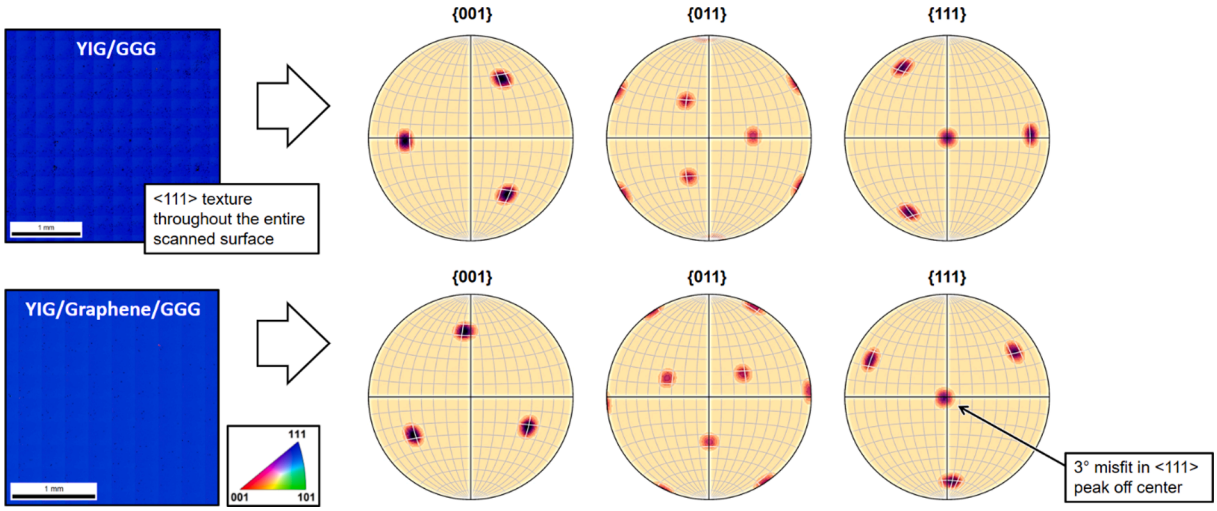

Fig. 8. (Left) surface EBSD reverse pole figure mapping of the YIG on bare and graphenated GGG showing uniform ⟨1 1 1⟩ texture throughout the entire observed area; (right) EBSD pole figures displaying {0 0 1}, {0 1 1} and {1 1 1} crystallographic plane markers for both YIG/GGG and YIG/Graphene/GGG samples, excellent texture along (1 1 1) direction is observed.

Resources. **J.L. McChesney:** Investigation. **F.M. Rodolakis:** Investigation. **M. van Veenendaal:** Software. **M. Velez:** Investigation. **R. Rao:** Investigation. **D. Haskel:** Investigation, Formal analysis. **J. Kim:** Resources. **A.N. Reed:** Resources. **M.R. Page:** Supervision, Funding acquisition.

Declaration of Competing Interest

The authors declare that they have no known competing financial interests or personal relationships that could have appeared to influence the work reported in this paper.

Acknowledgements

This work was partially supported by the Air Force Office of Scientific Research (AFOSR) Award No. FA955020RXCOR074. Use of the Advanced Photon Source at Argonne National Laboratory was supported by the U.S. Department of Energy, Office of Science, Office of Basic Energy Sciences, under Contract No. DE-AC02-06CH11357.

References

[1] C.W. Nan, M.I. Bichurin, S. Dong, D. Viehland, G. Srinivasan, Multiferroic magnetoelectric composites: Historical perspective, status, and future directions, J. Appl. Phys. 103 (2008), https://doi.org/10.1063/1.2836410, 031101.
[2] J. Ma, J. Hu, Z. Li, C.W. Nan, Recent Progress in Multiferroic Magnetoelectric Composites: from Bulk to Thin Films, Adv. Mater. 23 (9) (2011) 1062–1087, https://doi.org/10.1002/adma.201003636.
[3] H. Palneedi, V. Annapureddy, S. Priya, J. Ryu, Status and Perspectives of Multiferroic Magnetoelectric Composite Materials and Applications, Actuators. 5 (2016) 9, https://doi.org/10.3390/act5010009.
[4] Z. Chu, MohammadJavad PourhosseiniAsl, S. Dong, Review of multi-layered magnetoelectric composite materials and devices applications, J. Phys. Appl. Phys. 51 (24) (2018) 243001, https://doi.org/10.1088/1361-6463/aac29b.
[5] N.W. Emanetoglu, C. Gorla, Y. Liu, S. Liang, Y. Lu, Epitaxial ZnO piezoelectric thin films for saw filters, Mater. Sci. Semicond. Process. 2 (3) (1999) 247–252, https://doi.org/10.1016/S1369-8001(99)00022-0.
[6] H.P. Loebl, M. Klee, C. Metzmacher, W. Brand, R. Milsom, P. Lok, Piezoelectric thin AlN films for bulk acoustic wave (BAW) resonators, Mater. Chem. Phys. 79 (2-3) (2003) 143–146, https://doi.org/10.1016/S0254-0584(02)00252-3.
[7] W. Wang, P.M. Mayrhofer, X. He, M. Gillinger, Z. Ye, X. Wang, A. Bittner, U. Schmid, J.K. Luo, High performance AlScN thin film based surface acoustic wave devices with large electromechanical coupling coefficient, Appl. Phys. Lett. 105 (13) (2014), https://doi.org/10.1063/1.4896853, 133502.
[8] H. Greve, E. Woltermann, H.J. Quenzer, B. Wagner, E. Quandt, Giant magnetoelectric coefficients in (Fe90Co10)(78)Si12B10-AlN thin film composites, Appl. Phys. Lett. 96 (18) (2010), https://doi.org/10.1063/1.3377908, 182501.
[9] Z. Fang, S.G. Lu, F. Li, S. Datta, Q.M. Zhang, M. El Tahchi, Enhancing the magnetoelectric response of Metglas/polyvinylidene fluoride laminates by exploiting the flux concentration effect, Appl. Phys. Lett. 95 (11) (2009), https://doi.org/10.1063/1.3231614, 112903.
[10] J. Lou, R.E. Insignares, Z. Cai, K.S. Ziemer, M. Liu, N.X. Sun, Soft magnetism, magnetostriction, and microwave properties of FeGaB thin films, Appl. Phys. Lett. 91 (18) (2007) 182504, https://doi.org/10.1063/1.2804123.
[11] X. Liang, C. Dong, S.J. Celestin, X. Wang, H. Chen, K.S. Ziemer, M. Page, M. E. McConney, J.G. Jones, B.M. Howe, N.X. Sun, Soft Magnetism, Magnetostriction, and Microwave Properties of Fe-Ga-C Alloy Films, Ieee Magn. Lett. 10 (2019) 1–5, https://doi.org/10.1109/LMAG.2018.2889630.
[12] J. Wang, C. Dong, Y. Wei, X. Lin, B. Athey, Y. Chen, A. Winter, G.M. Stephen, D. Heiman, Y. He, H. Chen, X. Liang, C. Yu, Y. Zhang, E.J. Podlaha-Murphy, M. Zhu, X. Wang, J. Ni, M. McConney, J. Jones, M. Page, K. Mahalingam, N.X. Sun, Magnetostriction, Soft Magnetism, and Microwave Properties in Co-Fe-C Alloy Films, Phys. Rev. Appl. 12 (2019), https://doi.org/10.1103/PhysRevApplied.12.034011, 034011.
[13] Z. Wang, Y. Zhang, R. Viswan, Y. Li, H. Luo, J. Li, D. Viehland, Electrical and thermal control of magnetic coercive field in ferromagnetic/ferroelectric heterostructures, Phys. Rev. B. 89 (2014), https://doi.org/10.1103/PhysRevB.89.035118, 035118.
[14] X. Liang, H. Chen, N.X. Sun, Magnetoelectric materials and devices, Apl Mater. 9 (4) (2021), https://doi.org/10.1063/5.0044532, 041114.
[15] M. Weiler, L. Dreher, C. Heeg, H. Huebl, R. Gross, M.S. Brandt, S.T. B. Goennenwein, Elastically Driven Ferromagnetic Resonance in Nickel Thin Films, Phys. Rev. Lett. 106 (2011), https://doi.org/10.1103/PhysRevLett.106.117601, 117601.
[16] L. Dreher, M. Weiler, M. Pernpeintner, H. Huebl, R. Gross, M.S. Brandt, S.T. B. Goennenwein, Surface acoustic wave driven ferromagnetic resonance in nickel thin films: Theory and experiment, Phys. Rev. B. 86 (2012), https://doi.org/10.1103/PhysRevB.86.134415, 134415.
[17] D.A. Bas, P.J. Shah, A. Matyushov, M. Popov, V. Schell, R.C. Budhani, G. Srinivasan, E. Quandt, N. Sun, M.R. Page, Acoustically Driven Ferromagnetic Resonance in Diverse Ferromagnetic Thin Films, Ieee Trans. Magn. 57 (2) (2021) 1–5, https://doi.org/10.1109/TMAG.2020.3019214.
[18] D.A. Bas, P.J. Shah, M.E. McConney, M.R. Page, Optimization of acoustically-driven ferromagnetic resonance devices, J. Appl. Phys. 126 (11) (2019), https://doi.org/10.1063/1.5111846, 114501.
[19] H. Glass, M. Elliott, Attainment of Intrinsic Fmr Linewidth in Yttrium Iron-Garnet Films Grown by Liquid-Phase Epitaxy, J. Cryst. Growth. 34 (1976) 285–288, https://doi.org/10.1016/0022-0248(76)90141-X.
[20] V.V. Kruglyak, S.O. Demokritov, D. Grundler, Magnonics, J. Phys. Appl. Phys. 43 (26) (2010), https://doi.org/10.1088/0022-3727/43/26/264001, 264001.
[21] G. Schmidt, C. Hauser, P. Trempler, M. Paleschke, E.T. Papaioannou, Ultra Thin Films of Yttrium Iron Garnet with Very Low Damping: A Review, Phys. Status Solidi B-Basic Solid State Phys. 257 (7) (2020), https://doi.org/10.1002/pssb.v257.710.1002/pssb:201900644.
[22] B.M. Howe, S. Emori, H.M. Jeon, T.M. Oxholm, J.G. Jones, K. Mahalingam, Y. Zhuang, N.X. Sun, G.J. Brown, Pseudomorphic Yttrium Iron Garnet Thin Films With Low Damping and Inhomogeneous Linewidth Broadening, Ieee Magn. Lett. 6 (2015) 1–4, https://doi.org/10.1109/LMAG.2015.2449260.
[23] J.C. Gallagher, A.S. Yang, J.T. Brangham, B.D. Esser, S.P. White, M.R. Page, K. Y. Meng, S. Yu, R. Adur, W. Ruane, S.R. Dunsiger, D.W. McComb, F. Yang, P. C. Hammel, Exceptionally high magnetization of stoichiometric Y3Fe5O12 epitaxial films grown on Gd3Ga5O12, Appl. Phys. Lett. 109 (7) (2016), https://doi.org/10.1063/1.4961371, 072401.
[24] A.E. Clark, B. DeSavage, W. Coleman, E.R. Callen, H.B. Callen, Saturation Magnetostriction of Single-Crystal Yig, J. Appl. Phys. 34 (4) (1963) 1296–1297, https://doi.org/10.1063/1.1729480.
[25] Y.H. Rao, H.-W. Zhang, Q.H. Yang, D.N. Zhang, L.C. Jin, B.o. Ma, Y.J. Wu, Liquid phase epitaxy magnetic garnet films and their applications, Chin. Phys. B. 27 (8) (2018), https://doi.org/10.1088/1674-1056/27/8/086701, 086701.
[26] H. Chang, P. Li, W. Zhang, T. Liu, A. Hoffmann, L. Deng, M. Wu, Nanometer-Thick Yttrium Iron Garnet Films With Extremely Low Damping, Ieee Magn. Lett. 5 (2014) 1–4, https://doi.org/10.1109/LMAG.2014.2350958.
[27] F. Yang, P. Chris Hammel, FMR-driven spin pumping in Y3Fe5O12-based structures, J. Phys. Appl. Phys. 51 (25) (2018), https://doi.org/10.1088/1361-6463/aac249, 253001.
[28] Y. Sun, Y.Y. Song, H. Chang, M. Kabatek, M. Jantz, W. Schneider, M. Wu, H. Schultheiss, A. Hoffmann, Growth and ferromagnetic resonance properties of nanometer-thick yttrium iron garnet films, Appl. Phys. Lett. 101 (15) (2012), https://doi.org/10.1063/1.4759039, 152405.
[29] A.I. Stognij, N.N. Novitskii, S.A. Sharko, A.I. Serokurova, M.N. Smirnova, V. A. Ketsko, Growth and Properties of Y3Fe5O12 Films on LiNbO3 Substrates, Inorg. Mater. 56 (8) (2020) 847–853, https://doi.org/10.1134/S0020168520080154.
[30] H. Kum, D. Lee, W. Kong, H. Kim, Y. Park, Y. Kim, Y. Baek, S.H. Bae, K. Lee, J. Kim, Epitaxial growth and layer-transfer techniques for heterogeneous integration of materials for electronic and photonic devices, Nat. Electron. 2 (10) (2019) 439–450, https://doi.org/10.1038/s41928-019-0314-2.
[31] H.S. Kum, H. Lee, S. Kim, S. Lindemann, W. Kong, K. Qiao, P. Chen, J. Irwin, J. H. Lee, S. Xie, S. Subramanian, J. Shim, S.H. Bae, C. Choi, L. Ranno, S. Seo, S. Lee, J. Bauer, H. Li, K. Lee, J.A. Robinson, C.A. Ross, D.G. Schlom, M.S. Rzchowski, C. B. Eom, J. Kim, Heterogeneous integration of single-crystalline complex-oxide membranes, Nature. 578 (7793) (2020) 75–81, https://doi.org/10.1038/s41586-020-1939-z.
[32] Y. Kim, S.S. Cruz, K. Lee, B.O. Alawode, C. Choi, Y. Song, J.M. Johnson, C. Heidelberger, W. Kong, S. Choi, K. Qiao, I. Almansouri, E.A. Fitzgerald, J. Kong, A.M. Kolpak, J. Hwang, J. Kim, Remote epitaxy through graphene enables two-dimensional material-based layer transfer, Nature. 544 (7650) (2017) 340–343, https://doi.org/10.1038/nature22053.
[33] J.L. McChesney, R. Reininger, M. Ramanathan, C. Benson, G. Srajer, P. Abbamonte, J.C. Campuzano, The intermediate energy X-ray beamline at the APS, Nucl. Instrum. Methods Phys. Res. Sect. Accel. Spectrometers Detect. Assoc. Equip. 746 (2014) 98–105, https://doi.org/10.1016/j.nima.2014.01.068.
[34] S.S. Kalarickal, P. Krivosik, M. Wu, C.E. Patton, M.L. Schneider, P. Kabos, T. J. Silva, J.P. Nibarger, Ferromagnetic resonance linewidth in metallic thin films: Comparison of measurement methods, J. Appl. Phys. 99 (9) (2006), https://doi.org/10.1063/1.2197087, 093909.
[35] M.C. Onbasli, A. Kehlberger, D.H. Kim, G. Jakob, M. Kläui, A.V. Chumak, B. Hillebrands, C.A. Ross, Pulsed laser deposition of epitaxial yttrium iron garnet films with low Gilbert damping and bulk-like magnetization, Apl Mater. 2 (10) (2014), https://doi.org/10.1063/1.4896936, 106102.
[36] J.H. Sinfelt, G.D. Meitzner, X-Ray Absorption-Edge Studies of the Electronic-Structure of Metal-Catalysts, Acc. Chem. Res. 26 (1) (1993) 1–6, https://doi.org/10.1021/ar00025a001.
[37] F.M.F. de Groot, X-Ray-Absorption and Dichroism of Transition-Metals and Their Compounds, J. Electron Spectrosc. Relat. Phenom. 67 (4) (1994) 529–622, https://doi.org/10.1016/0368-2048(93)02041-J.
[38] M. Sassi, C.I. Pearce, P.S. Bagus, E. Arenholz, K.M. Rosso, First-Principles Fe L-2, L-3-Edge and O K-Edge XANES and XMCD Spectra for Iron Oxides, J. Phys. Chem. A. 121 (2017) 7613–7618, https://doi.org/10.1021/acs.jpca.7b08392.
[39] Y.Y. Chin, H.J. Lin, Y.F. Liao, W.C. Wang, P. Wang, D. Wu, A. Singh, H.Y. Huang, Y. Y. Chu, D.J. Huang, K.D. Tsuei, C.T. Chen, A. Tanaka, A. Chainani, Local spin moments, valency, and long-range magnetic order in monocrystalline and ultrathin films of Y3Fe5O12 garnet, Phys. Rev. B. 99 (2019), https://doi.org/10.1103/PhysRevB.99.184407, 184407.
[40] Michel van Veenendaal, private communication, (n.d.).

[41] H. Maier-Flaig, S. Klingler, C. Dubs, O. Surzhenko, R. Gross, M. Weiler, H. Huebl, S. T.B. Goennenwein, Temperature-dependent magnetic damping of yttrium iron garnet spheres, Phys. Rev. B. 95 (2017), https://doi.org/10.1103/PhysRevB.95.214423, 214423.
[42] M. Sparks, Ferromagnetic-relaxation theory, McGraw-Hill, New York, 1964.
[43] A.C. Ferrari, D.M. Basko, Raman spectroscopy as a versatile tool for studying the properties of graphene, Nat. Nanotechnol. 8 (4) (2013) 235–246, https://doi.org/10.1038/nnano.2013.46.
[44] J.B. Wu, M.L. Lin, X. Cong, H.N. Liu, P.H. Tan, Raman spectroscopy of graphene-based materials and its applications in related devices, Chem. Soc. Rev. 47 (5) (2018) 1822–1873.
[45] G.A. McQuade, A.S. Plaut, A. Usher, J. Martin, The thermal expansion coefficient of monolayer, bilayer, and trilayer graphene derived from the strain induced by cooling to cryogenic temperatures, Appl. Phys. Lett. 118 (20) (2021), https://doi.org/10.1063/5.0035391, 203101.
[46] T.B. Britton, J. Jiang, Y. Guo, A. Vilalta-Clemente, D. Wallis, L.N. Hansen, A. Winkelmann, A.J. Wilkinson, Tutorial: Crystal orientations and EBSD - Or which way is up? Mater. Charact. 117 (2016) 113–126, https://doi.org/10.1016/j.matchar.2016.04.008.